Photoelectric Energy Conversion of Plasmon-Generated Hot Carriers in Metal–Insulator–Semiconductor Structures

F. Pelayo García de Arquer, Agustín Mihi, Dominik Kufer, and Gerasimos Konstantatos*

ICFO—Institut de Ciències Fotòniques, Mediterranean Technology Park, 08860 Castelldefels, Barcelona, Spain

ABSTRACT Plasmonic excitation in metals has received great attention for light localization and control of light-matter interactions at the nanoscale with a plethora of applications in absorption enhancement, surface-enhanced Raman scattering, or biosensing. Electrically active plasmonic devices, which had remained underexplored, have recently become a growing field of interest. In this report we introduce a metal–insulator–semiconductor heterostructure for plasmo-electric energy conversion, a novel architecture to harvest hot-electrons derived from plasmonic excitations. We demonstrate external quantum efficiency (EQE) of 4% at 460 nm using a Ag nanostructured electrode and EQE of 1.3% at 550 nm employing a Au nanostructured electrode. The insulator interfacial layer has been found to play a crucial role in interface passivation, a requisite in photovoltaic applications to achieving both high open-circuit voltages (0.5 V) and fill-factors (0.5), but its introduction simultaneously modifies hot-electron injection and transport. We investigate the influence passivation has on these processes for different material configurations, and characterize different types of transport depending on the initial plasmon energy band, reporting power conversion efficiencies of 0.03% for nanopatterned silver electrodes.

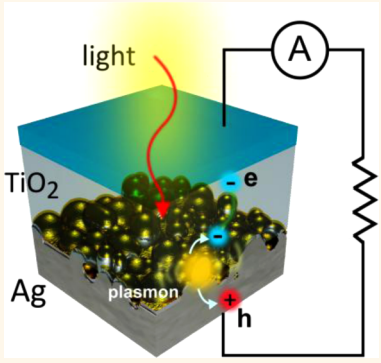

KEYWORDS: plasmonics · hot-electron · solar cell · metal–insulator-semiconductor

Plasmonic structures offer unique capabilities to control light-matter interaction in the nanoscale.[1] The ability to manipulate photon absorption, emission, and localization to artificially modify the photonic density of states in such structures is of great interest for several applications such as sensing, medicine, quantum optics and energy conversion.[2−5] Once a plasmonic mode has been excited, it can be damped through a number of pathways: reradiation or scattering of light, and the promotion of electrons to the conduction band of the metal.[6] These excited electrons lose their energy by electron–electron or electron–phonon scattering, resulting in dissipation of heat to the structure.[7,8] The latter is a lossy phenomenon which has impeded the use of metals from effectively harvesting light. However, in the presence of a Schottky junction in the vicinity of hot carrier generation, it has been shown that their collection is possible before cooling *via* tunneling through the Schottky barrier.[9,10]

Plasmonic resonances in metals depend both on material properties and geometry. In particular, metal nanostructures support localized surface plasmon resonances (LSPRs). These collective electron oscillations introduce highly tunable additional quantized electronic states, whose tailored absorption is followed by the creation of very strong and localized electromagnetic fields.[1] These phenomena have been widely employed in optoelectronics to improve the performance of solar cells and photodetectors, relying on the increased optical absorption in the vicinity of such structures. Unlike semiconductors, where light is absorbed within a thickness of 1 μm (for direct bandgap semiconductors) to 100 μm (for indirect-bandgap semiconductors), appropriately designed metal nanostructures exhibit total light absorption within thicknesses below 90 nm[11−14] or show omnidirectional coupling.[15] The direct use of LSPRs to harvest light would open the exciting possibility of creating artificial materials with

* Address correspondence to gerasimos.konstantatos@icfo.es.

Received for review January 31, 2013 and accepted March 17, 2013.

Published online March 17, 2013
10.1021/nn400517w

© 2013 American Chemical Society

a tailored absorption, but without the bandgap limitations of bulk semiconducting materials.[9]

The injection of excited electrons from metal nanoparticles into high band gap semiconductors has been demonstrated to be an efficient process.[16] On that basis, metal nanostructures have been employed in photocatalytic devices and dye-sensitized solar cells.[17,18] Solid-state photodetectors relying on hot-electron harnessing have also been reported utilizing tunable resonant nanoantennas for hot-electron transfer from gold antennas to Si or graphene.[9,19] Nishijima *et al.* reported TiO_2/Au Schottky electrolyte-based diodes, where hot-electrons are transferred to TiO_2 from Au nanoantennas which were regenerated in the presence of an electrolyte.[17] Patterning the metal electrode, Lee and co-workers studied hot-electron injection in TiO_2/Au diodes.[10] A detailed study of plasmonic photosensitization of a TiO_2 photoconductor with embedded Au nanoparticles (NPs) was also reported, relating the dependence of hot-electron transfer with absorption in the NPs, and calculating the effective dielectric constants of the resulting composites.[20] Recently, the effect of metal nanoparticles as sensitizers in TiO_2/spiro-O-MeTad device was reported as a solid-state alternative.[21] The possibility of collecting the hot electrons in structures other than Schottky junctions was presented by Wang *et al.*[22] The authors present a complete theoretical analysis of metal−insulator−metal (MIM) devices, where excited surface plasmon polaritons provided by a Kretschmann coupling mechanism result in hot electrons tunneling through the insulator barrier. In sum, to date, photoconductors, Schottky, and MIM diodes showing plasmonic-based hot-carrier generation have been reported as a promising route toward energy harvesting. However, important figures of merit for solar cells such as open-circuit voltage (V_{oc}) and fill factor (FF) and their origin of optimization have largely remained unexplored. In this work we report a novel architecture to harvest solar energy with the use of hot-carriers derived from the plasmonic excitation of metal nanostructures, and investigate the crucial role of the metal−semiconductor interface in transport to achieve high V_{oc} and FF.

RESULTS AND DISCUSSION

We demonstrate here all-solid state hot-electron based solar cells, consisting of a high bandgap semiconductor (TiO_2) Schottky junction with a nanotextured metal contact. To take advantage of excited hot-electrons a number of conditions need to be simultaneously satisfied: (*i*) an incident light to LSPR efficient coupling structure compatible with device architecture, (*ii*) a static electric field to separate plasmonically created electron−hole pairs in the metal before they thermalize, and (*iii*) a passivation layer in the interface to reduce recombination and control the junction. In the present work we rely on TiO_2 nanotextured films to pattern a top-evaporated metallic contact, in such a way that metal serves both as a source of hot-electron generation and as the cathode. Alumina (Al_2O_3) barriers have been widely used to reduce recombination in dye sensitized solar cells.[23,24] To mitigate recombination due to traps at the interface, we introduce a passivation layer of alumina between them and study the effect on hot electron transfer and device performance, depending on the LSPR excitation for different metals.

The schematic of the reported structures is shown in Figure 1. TiO_2 films are deposited on top of transparent conducting oxides. Flat devices (Figure 1a) consist of 50 nm of TiO_2 (anatase) deposited by atomic layer deposition (ALD) on top of an indium tin oxide (ITO) flat film and were used as control devices. Nanotextured devices are fabricated from TiO_2 nanocrystals spin-coated on top of a fluorine tin oxide (FTO) electrode (see Materials and Methods section). The morphology of the resulting films prior to metal deposition is shown in Figure 1c,d, as characterized by atomic force microscopy (AFM), revealing random features of around 80 nm height in the patterned devices as opposed to the flat control ones. After metal evaporation, the contacts follow TiO_2 roughness, thus being flat or textured depending on the substrate. The absorption of patterned and flat electrodes deposited over glass is shown in Figure 1e,f. Nanotextured metal−semiconductor structures provide much higher coupling efficiency, showing a resonance peak around 475 nm. Flat films on the other hand do not exhibit such a large absorption or a well-defined plasmon resonance, which is also supported by numerical simulations (see Supporting Information, section S1). This difference can also be visually inspected by looking at the back of the metal contacts (Figure 1e,f insets). The gray, metallic-like reflection from the back of the flat contact is in accordance with a reflection from a flat metallic silver surface. Nanotextured samples exhibit yellow-orange colors, indicative of increased in-coupling and a modified plasmon resonance due to film roughness. The external quantum efficiency (EQE), which is the number of generated carriers per incident photon (also called IPCE—incident photon to carrier conversion), of textured and flat devices is shown in Figure 1e,f, respectively. Patterned devices show a well-defined resonance close to 460 nm, in agreement with the absorption profile of similar films, whereas the EQE of flat devices does not show any resonance but instead follows a Fowler law (see Supporting Information, section S2).

A hot-carrier photocurrent is obtained when energetic electrons derived from LSPR damping are emitted over or tunnel to the semiconductor (Figure 2a dashed lines). This mechanism has three competitive processes, which might impede electrons in the metal from reaching the TiO_2. Excited electrons can be lost *via* intraband thermalization (dashed arrows Figure 2a,d), interband transitions, or surface recombination at the

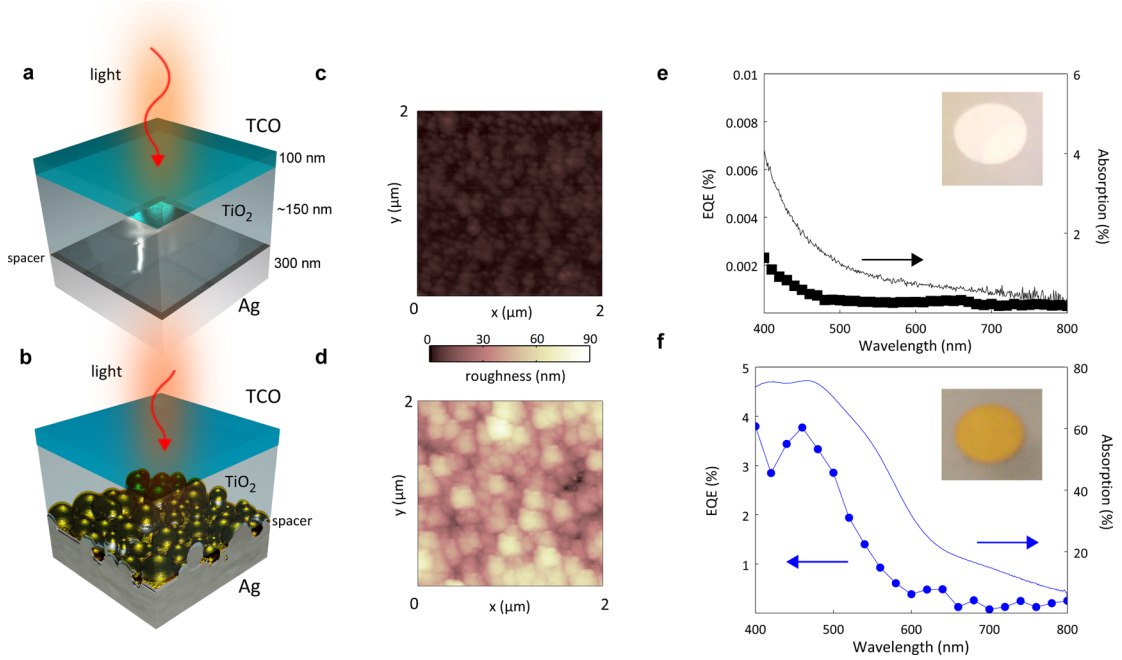

Figure 1. Flat and nanopatterned device structures. Flat control device structure consisting of ITO–TiO_2–Al_2O_3–Ag layers: (a) schematic and (c) AFM image. Nanopatterned device structure consists of FTO–TiO_2–Al_2O_3–Ag layers: (b) schematic and (d) AFM image. Typical dimensions included in panel a. EQE (marked lines) and absorption (solid lines) in the metal for similar films on glass, both for flat device (e) and patterned device without spacer (f). The insets show photographs of the metal contact as seen through the TiO_2, illustrating the difference of flat and nanopatterned metal electrodes and the arising plasmon resonance.

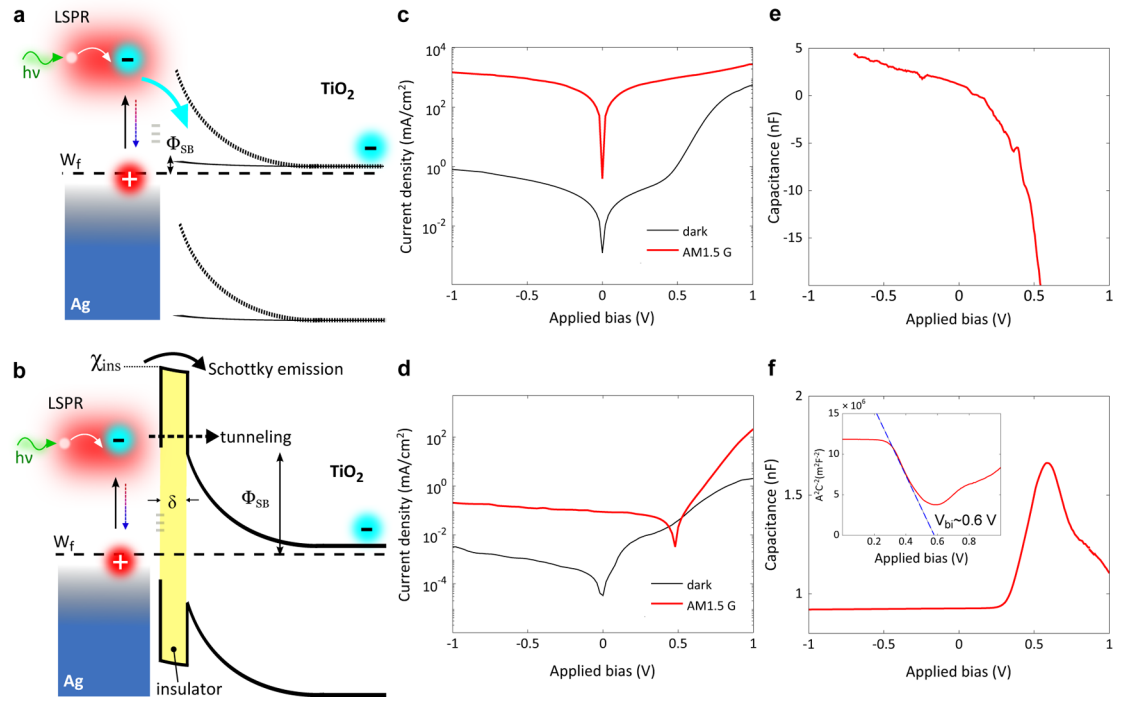

Figure 2. The effect of the interface on the junction properties and resultant *I*–*V* characteristics. LSPR excited by an incoming photon can result in the creation of an electron–hole pair, which can be split by the built-in field in the interface. Un-passivated interfaces (a) contain traps that can result in Fermi level pinning deteriorating the junction from the ideal case (solid versus dashed lines, respectively). This results in a suppression of open-circuit voltage (V_{oc}) and no power conversion efficiency (PCE) (c). Passivation of interface states prevents pinning (b). Depending on their energy, the excited electrons can either tunnel to the TiO_2 or undergo Schottky emission over the barrier. The height of the barrier determines the difference of metal work-function (W_f) and insulator electron affinity (χ_{ins}). (d) Current–voltage characteristics in dark and under simulated AM1.5G solar illumination of a typical passivated device with 1 nm of alumina. Capacitance–voltage spectroscopy of un-passivated devices (e) and passivated devices (f) revealing the appearance of a built-in potential (Mott–Schottky analysis shown in the inset).

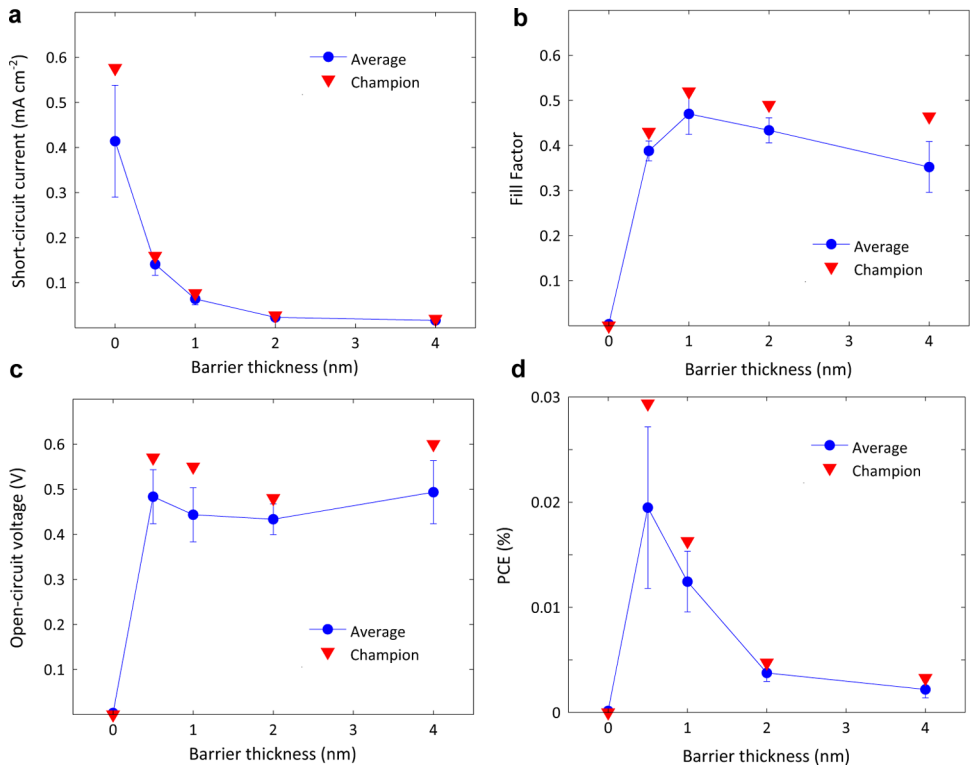

Figure 3. Solar cell parameters as a function of Al_2O_3 thickness (δ) for Ag electrodes. (a) Short-circuit current (J_{sc}), (b) fill-factor (FF), (c) V_{oc}, and (d) PCE. Error bars correspond to the standard deviation and an average in the plotted parameter for at least five similar devices. Champion values for each parameter are also shown (triangle marker). A maximum PCE of 0.029% is found for δ = 0.5 nm.

interface.[6,22] The first two processes are intrinsic to both metal and geometry,[25] whereas the third factor can be mitigated by controlling the passivation at the interface. The current–voltage characteristic of the device shows very high photocurrent despite the absence of photovoltaic effect (Figure 2c). Without a protective barrier (Figure 2a solid lines), the Ag-TiO_2 interface surface states result in Fermi level pinning and a reduced built-in potential compared to the theoretical one, which would be derived from the difference of metal workfunction and semiconductor Fermi level.[26] To further corroborate the origin of open-circuit-voltage and the effect of Al_2O_3 passivation, we performed capacitance–voltage spectroscopy of these devices (Figure 2e,f). This reveals that, in the absence of the insulator layer (Figure 2e), the built-in field vanishes which results in the absence of open-circuit voltage. The effect of the Al_2O_3 layer (Figure 2f) leads however to built-in potentials on the order of 600 mV (see Mott–Schottky plot in the inset). This value comprises both the Schottky barrier (Φ_{SB}) in the semiconductor and the voltage drop across the insulator.[26,27] In the current structure, electron–hole pairs derived from LSPR are split when, depending on their energy, electrons tunnel through or are emitted over the Al_2O_3 barrier. It should be noted that in our structures hot-carriers generated in the metal and transferred to the titania rapidly thermalize in the titania to the conduction band, giving rise to open circuit voltage determined by the built-in electric field of the junction. Current–voltage characteristics of a typical device with 1 nm of Al_2O_3 barrier are shown in Figure 2d, in dark and under AM1.5G simulated illumination, demonstrating the ability of these metal–insulator–semiconductor (MIS) devices to harvest solar energy and convert it to electricity. To experimentally assess the contribution of plasmonic hot-electrons in the total PCE, we performed measurements under solar irradiation employing various filtering conditions to eliminate photon absorption from the TiO_2 phase in the devices. In doing so we find that ~80% of J_{sc} is attributed to hot electron generation (see Supporting Information, section S3) and the titania contributes with ~20% in the case of Ag-based devices.

The influence of the insulator layer thickness (δ), which determines the transfer of hot-carriers to TiO_2, on device performance is studied in Figure 3, resulting in an optimized device architecture. Short circuit current density (panel a) increases with decreasing δ, indicative of a more efficient transfer of the excited hot electrons to the semiconductor. This is maximum in the absence of the Al_2O_3 barrier, but as previously discussed, Fermi-level pinning results in a tiny V_{oc} and no net PCE. No appreciable difference is observed for the dependence of FF and V_{oc} on δ. For increasing values of δ, FF marginally decreases due to increasing sheet resistance of the thicker Al_2O_3 film.[27] We find that the dependence of the PCE with thickness is strongly correlated with J_{sc}, provided there is no Fermi-level

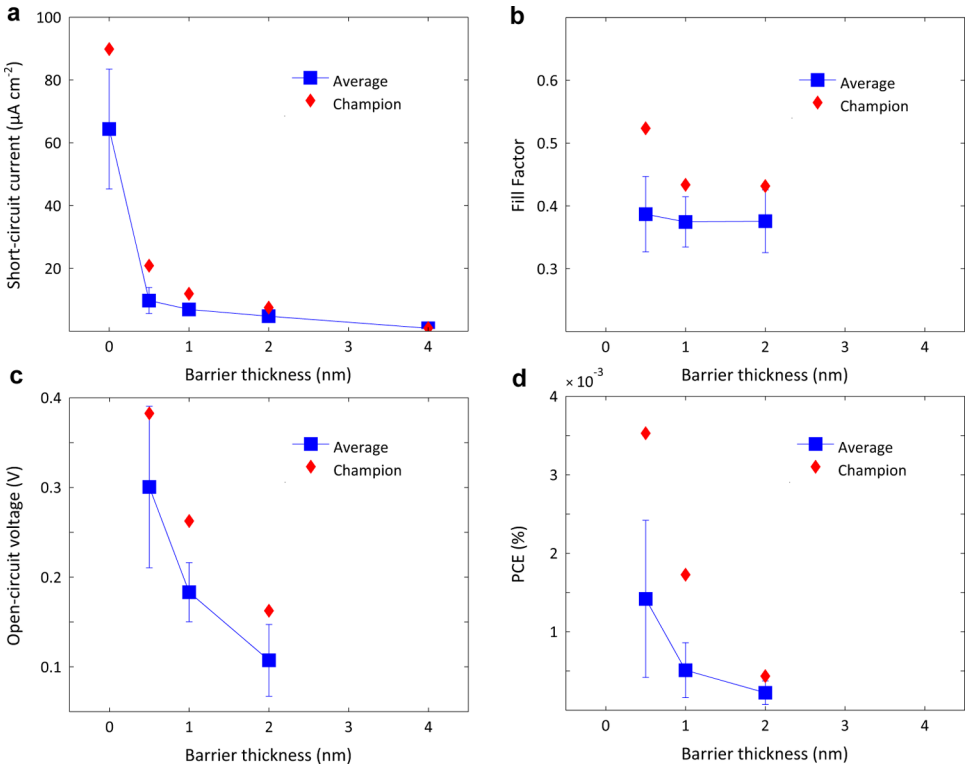

Figure 4. Solar cell parameters as a function of Al_2O_3 thickness (δ) for Au electrodes. (a) Short-circuit current (J_{sc}), (b) fill-factor (FF), (c) V_{oc} and (d) PCE. Error bars correspond to the standard deviation and an average in the plotted parameter for at least five similar devices. Champion values for each parameter are also shown (diamond marker). For δ = 4 nm the tunneling current is negligible and the subsequent parameters omitted in the plots.

pinning. The maximum PCE = 0.029% is found for δ = 0.5 nm devices, with short-circuit current density (J_{sc}) of 0.14 mA cm^{-2}, V_{oc} of 0.48 V, and fill-factor of 0.46.

The spectral harnessing potential of these structures can be selected by the choice of the metal and/or geometry, which will modify both the electrical and optical properties of the devices, due to the change in workfunction, and the shift of the corresponding plasmon resonance. We proceed now to study the effect of the alumina layer for gold electrodes (Figure 4). Capacitance−voltage spectroscopy measurements of these devices (see Supporting Information, section S4) reveal a reduced built-in potential, around 300 meV, as compared to 500−600 meV for silver. These lower built-in potentials are subsequently accompanied by lower open-circuit voltages (Figure 4c). Short-circuit currents (Figure 4a) are also lower in this scenario (around one order of magnitude), and increase with decreasing alumina thickness as in the silver case. Despite a similar trend in efficiency with thickness, it is evident that both the electronic properties and the plasmo-electric conversion performance of devices with gold electrodes are different compared to silver. By studying the bias dependence of hot-electron injection in both scenarios we attribute the origin of these differences to the different types of electron transport through the interface in both configurations.

The EQE of Ag-based devices is shown in Figure 5a, to illustrate their bias dependence. It is worth noting the difference in amplitude of the EQE of these devices (with Al_2O_3 barrier) with the EQE of the device in Figure 1f (without Al_2O_3 barrier). This comes as a consequence of the introduction of the thin alumina barrier, which reduces the efficiency of the hot carrier injection. The EQE in this case is weakly dependent on the external bias as shown in Figure 5a, which could indicate thermionic emission as the main mechanism of electron transfer; photoexcited electrons in the Ag have energies near the band-edge of the alumina barrier. The height of the Ag−Al_2O_3 barrier can be estimated *via* photoemission by fitting the obtained spectrum from a flat device.[26] This yields an effective barrier of approximately 2 eV (see Supporting Information, section S2), which is in good agreement with the difference of Al_2O_3 electron affinity, taken from other studies for a similar fabrication process,[28] and the reported values of the workfunction of Ag (∼4.7 eV). The thermionic emission transport is further supported by the observed dependence of the photocurrent for nanopatterned devices at short-circuit conditions, which depends on the square root of barrier thickness following a law $I \propto \exp(-a\delta^{1/2})$,[29] (see Supporting Information, section S5).

The case of gold (Figure 5b) is different, showing a pronounced bias dependence on EQE. In the absence of bias, the EQE of these devices is roughly one order of magnitude smaller than for silver, which is in

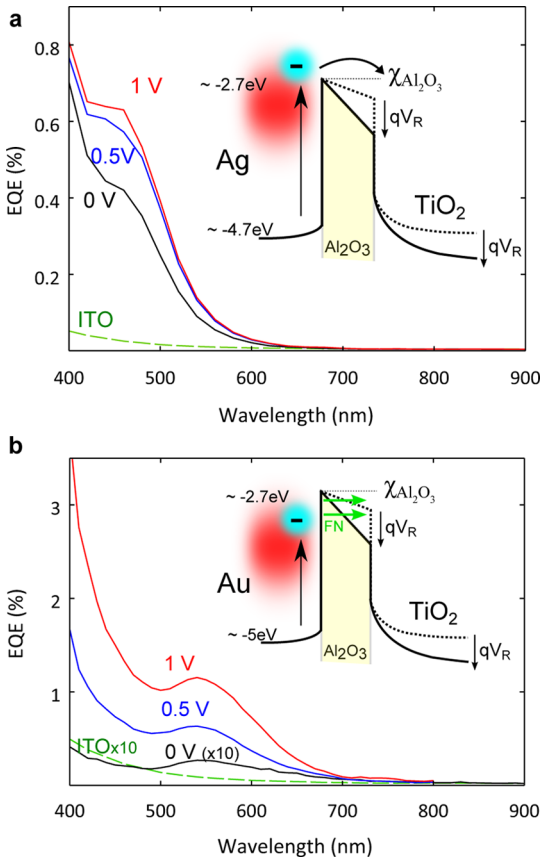

Figure 5. Comparison of silver and gold and the effect of reverse bias (V_R). (a) Silver and (b) gold. Note gold EQE at 0 V has been scaled (×10) to facilitate interpretation. Schematics illustrating the transport properties for each configuration are shown in the respective insets. Electrons derived from Ag LSPR can be emitted over the barrier, whereas Au LSPR electrons will undergo Fowler–Nordheim tunneling. The EQE of devices with ITO electrodes is shown for comparison, to discard TiO_2 midgap states as the origin of photosensitization.

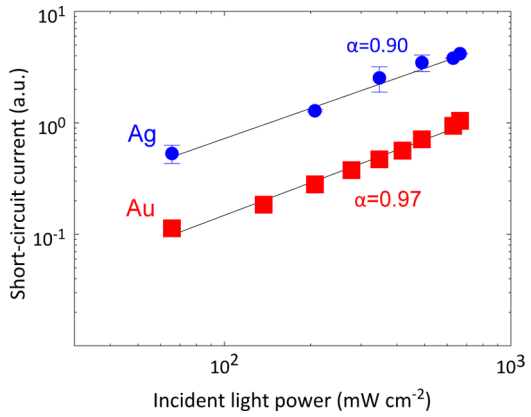

Figure 6. Short-circuit current dependence with incident light intensity for gold and silver. Statistics also included for at least three different measurements (when not shown error-bars smaller than the corresponding symbol). The data are linearly fitted, the slope α yielding the power law dependence of the current ($I \propto P^{\alpha}$).

agreement with the reduced J_{sc} and PCE shown in Figure 4. In the presence of reverse bias the EQE for gold devices is markedly increased, from roughly 0.03% up to around 1.3% at the plasmon resonance for 1 V of reverse bias. The different behavior compared to silver can be accounted for by the different nature of electron transport across the insulator. In this case it is found that the dominant mechanism is Fowler–Nordheim field-assisted transport.[26] This type of transport obeys an exponential dependence law of the type $I \propto \exp(-a\delta)$ with barrier thickness,[29] which is in excellent agreement with the fits of the experimental photocurrents at short-circuit conditions and 635 nm illumination for different barriers (see Supporting Information, section S6).

To eliminate possible midgap states in the titania as the source of visible photosensitization in these devices we fabricated devices in which the metal has been replaced by a transparent conductive oxide (ITO). Figure 5 shows the spectral EQE of these structures and the absence of visible response as opposed to the case of metal-based structures demonstrates the plasmonic generation of hot carriers in the metal as the source of the sensitization in those devices.

Intensity dependent measurements of short-circuit current are shown in Figure 6. A linear law between short-circuit current and incident light power ($I \propto P^{\alpha}$) is expected for generation-limited devices. In our case both silver ($\alpha \approx 0.90$) and gold ($\alpha \approx 0.97$) are close to unity, suggestive of the absence of space charge formation as the limiting factor in the performance of these devices.[30] An additional asset of these plasmonic-based devices is their potentially superior long-term stability compared to other technologies.[21] In our architectures, silver devices are stable within 22% performance degradation after 2 months of storage (Supporting Information, section S7).

CONCLUSIONS

The major roadblock toward higher performance stems from the low quantum efficiency of this architecture. This initially modest number, far from the injection yield obtained in similar processes,[16] might have its origin in a combination of the following: (i) a poor efficiency of electron–hole generation over photon reradiation for LSPR damping in the current structure,[6] (ii) small tunneling probability, and (iii), cooling and recombination rates of electrons in the metal faster than the tunneling rate into the semiconductor.[7] These limits could be surmounted with the use of more complex metallic structures, with tailored photonic density of states able to increase the plasmon to hot-electron conversion efficiency, and by manipulating the interface electronic properties. A proper design of the plasmonic nanostructures can modify the rates of radiative and Landau damping mechanisms, resulting in favorable hot electron generation.[6,7] The use of structures supporting Fano resonances could also reduce reradiation channels increasing hot electron generation rates.[19] Engineered geometries seeking to improve hot-electron

collection from emitting nanostructures and the research of novel passivating layers will also open exciting opportunities to control the transport and electronic properties of these devices toward simultaneous achievement of high quantum efficiency, open-circuit voltage and fill-factor.

MATERIALS AND METHODS

Device fabrication. ITO-coated glass substrates were purchased from Stuttgart University and were cleaned with acetone, ethanol, and DI water under sonication 10 min each in sequence before use. FTO-coated glass substrates were purchased from Xop Fisica and cleaned with the same procedure. TiO_2 films were deposited on top of FTO substrates as reported elsewhere.[31] Flat devices were fabricated by atomic layer deposition (ALD) of 50 nm of TiO_2 over ITO substrates. TiO_2 and Al_2O_3 were deposited by atomic layer deposition (Savannah 200, Cambridge Nanotech). Water and trimethylaluminium were used as precursors of Al_2O_3 with open valve times of 0.05 and 0.10 s, respectively, followed by 65 s pump time (1.1 A per cycle). The chamber was kept at 150 °C during the deposition process. TiO_2 coatings were fabricated from water and titanium isopropoxide; valves were set to 0.015 and 0.065 s, respectively, followed by 10 s pump time (0.025 A per cycle). The deposition chamber temperature was held at 200 °C. All TiO_2 substrates were heated at 120 °C for 30 min to remove moisture traces prior to ALD. There was 300 nm of metal deposited on a Kurt J. Lesker Nano 36 system at a rate of 0.5 Å s^{-1} for the first 30 nm and 1.5 Å s^{-1} for the remaining 250 nm, at a base pressure lower than 2×10^{-6} mbar. Final thickness was controlled together with deposition rate monitoring *via* a quartz crystal. A 200 nm thick ITO film was deposited by DC magnetron sputtering (AJA International Orion 8) at room temperature. The sputtering was carried out at 60W DC-power and at a working pressure of 2 mTorr in a 5% in oxygen argon atmosphere. A shadow mask with circles of 2 mm diameter was used to define the contact pads area.

Device Characterization. All device characterization was performed in ambient conditions. Current–voltage characteristics were recorded using a Keithley 2400 source meter. Illumination intensity of AM 1.5 was accomplished using a solar simulator (Newport Oriel Sol3A class AAA). A shadow mask was placed just before our device so that incident light area matches with the device area. To avoid charging/discharging during EQE measurements, devices were illuminated by a Newport Cornerstone 260 monochromator modulated with a 20 Hz chopper, and the short circuit current measured with a Stanford Research System SR830 Lock-In amplifier, in series with a 500 Ω resistor and a Keithley 2400 to establish the voltage across the devices. To avoid impedance mismatches, the obtained spectra were normalized accordingly to the obtained responsivities under a 406 nm laser illumination with a frequency of 50 mHz and a power density of 2 mW/cm^2, measured with a Keithley 2636 source meter. Short-pulsed and continuous-wave illumination at 406 and 635 nm was achieved by controlling a 4-channel LASER with an Agilent 33220A waveform generator.

Absorption Measurements. Total absorption of our films was measured using a Cary 5000 UV–vis–NIR spectrophotometer with an integrating sphere attachment. The size of the samples was increased to 1 in. × 1 in. to match reflection and transmission ports.

Atomic Force Microscopy. Atomic force microscopy (AFM) studies were carried out using a tapping mode Vecco Dimension 3100 system.

Capacitance–Voltage Spectroscopy. Capacitance–voltage characteristics were measured using an Agilent E4980A LCR meter, with an AC signal modulation of 1 kHz and 50 mV amplitude.

Finite-Difference Time-Domain Simulations. Finite-difference time-domain simulations (FDTD) were carried out using Lumerical FDTD solutions suite version 8 (http://www.lumerical.com).

Conflict of Interest: The authors declare no competing financial interest.

Acknowledgment. This research has been supported by Fundació Privada Cellex Barcelona, the European Commission's Seventh Framework Programme for Research under Contract PIRG06-GA-2009-256355 and the Ministerio de Ciencia e Innovación under Contract No. TEC2011-24744. The authors thank L. Martinez for assistance with the atomic force microscope and F. Beck for useful discussions.

Supporting Information Available: FDTD simulations, capacitance–voltage measurements, estimation of barrier height, estimation of TiO_2 contribution to short-circuit current, and characterization of hot-electron transport. This material is available free of charge *via* the Internet at http://pubs.acs.org.

REFERENCES AND NOTES

1. Schuller, J. A.; Barnard, E. S.; Cai, W.; Jun, Y. C.; White, J. S.; Brongersma, M. L. Plasmonics for Extreme Light Concentration and Manipulation. *Nat. Mater.* **2010**, *9*, 193–204.
2. Jin, Y. Engineering Plasmonic Gold Nanostructures and Metamaterials for Biosensing and Nanomedicine. *Adv. Mater.* **2012**, *24*, 5153–5165.
3. Zheng, Y. B.; Kiraly, B.; Weiss, P. S.; Huang, T. J. Molecular Plasmonics for Biology and Nanomedicine. *Nanomedicine* **2012**, *7*, 751–770.
4. Atwater, H. A.; Polman, A. Plasmonics for Improved Photovoltaic Devices. *Nat. Mater.* **2010**, *9*, 205–213.
5. Juan, M. L.; Righini, M.; Quidant, R. Plasmon Nano-optical Tweezers. *Nat. Photon.* **2011**, *5*, 349–356.
6. Sönnichsen, C.; Franzl, T.; Wilk, T.; Plessen, G.; von Feldmann, J. Drastic Reduction of Plasmon Damping in Gold Nanorods. *Phys. Rev. Lett.* **2002**, *88*, 077402.
7. Hartland, G. V. Optical Studies of Dynamics in Noble Metal Nanostructures. *Chem. Rev.* **2011**, *111*, 3858–3887.
8. Voisin, C.; Fatti, N.; Del Christofilos, D.; Vallée, F. Ultrafast Electron Dynamics and Optical Nonlinearities in Metal Nanoparticles. *J. Phys. Chem. B* **2001**, *105*, 2264–2280.
9. Knight, M. W.; Sobhani, H.; Nordlander, P.; Halas, N. J. Photodetection with Active Optical Antennas. *Science* **2011**, *332*, 702–704.
10. Lee, Y. K.; Jung, C. H.; Park, J.; Seo, H.; Somorjai, G. A.; Park, J. Y. Surface Plasmon-Driven Hot Electron Flow Probed with Metal-Semiconductor Nanodiodes. *Nano Lett.* **2011**, *11*, 4251–4255.
11. Kravets, V.; Schedin, F.; Grigorenko, A. Plasmonic Blackbody: Almost Complete Absorption of Light in Nanostructured Metallic Coatings. *Phys. Rev. B* **2008**, *78*, 205405.
12. Fang, Z.; Zhen, Y.-R.; Fan, L.; Zhu, X.; Nordlander, P. Tunable Wide-Angle Plasmonic Perfect Absorber at Visible Frequencies. *Phys. Rev. B* **2012**, *85*, 245401.
13. Tittl, A.; Mai, P.; Taubert, R.; Dregely, D.; Liu, N.; Giessen, H. Palladium-Based Plasmonic Perfect Absorber in the Visible Wavelength Range and Its Application to Hydrogen Sensing. *Nano Lett.* **2011**, *11*, 4366–4369.
14. Liu, N.; Mesch, M.; Weiss, T.; Hentschel, M.; Giessen, H. Infrared Perfect Absorber and Its Application as Plasmonic Sensor. *Nano Lett.* **2010**, *10*, 2342–2348.
15. Teperik, T. V.; García de Abajo, F. J.; Borisov, A. G.; Abdelsalam, M.; Bartlett, P. N.; Sugawara, Y.; Baumberg, J. J. Omnidirectional Absorption in Nanostructured Metal Surfaces. *Nat. Photon.* **2008**, *2*, 299–301.
16. Furube, A.; Du, L.; Hara, K.; Katoh, R.; Tachiya, M. Ultrafast Plasmon-Induced Electron Transfer from Gold Nanodots into TiO_2 Nanoparticles. *J. Am. Chem. Soc.* **2007**, *129*, 14852–14853.
17. Nishijima, Y.; Ueno, K.; Yokota, Y.; Murakoshi, K.; Misawa, H. Plasmon-Assisted Photocurrent Generation from Visible to Near-Infrared Wavelength Using a Au-Nanorods/TiO_2 Electrode. *J. Phys. Chem. Lett.* **2010**, *1*, 2031–2036.

18. Lenzmann, F. O.; O'Regan, B. C.; Smits, J. J. T.; Kuipers, H. P. C. E.; Sommeling, P. M.; Slooff, L. H.; Roosmalen, J. A. M. van Dye Solar Cells without Electrolyte or Hole-Transport Layers: A Feasibility Study of a Concept Based on Direct Regeneration of the Dye by Metallic Conductors. *Prog. Photovol. Res. Appl.* **2005**, *13*, 333–340.
19. Fang, Z.; Liu, Z.; Wang, Y.; Ajayan, P. M.; Nordlander, P.; Halas, N. J. Graphene-Antenna Sandwich Photodetector. *Nano Lett.* **2012**, *12*, 3808–3813.
20. Mubeen, S.; Hernandez-Sosa, G.; Moses, D.; Lee, J.; Moskovits, M. Plasmonic Photosensitization of a Wide Band Gap Semiconductor: Converting Plasmons to Charge Carriers. *Nano Lett.* **2011**, *11*, 5548–5552.
21. Reineck, P.; Lee, G. P.; Brick, D.; Karg, M.; Mulvaney, P.; Bach, U. A Solid-State Plasmonic Solar Cell *via* Metal Nanoparticle Self-Assembly. *Adv. Mater.* **2012**, *24*, 4750–4755.
22. Wang, F.; Melosh, N. A. Plasmonic Energy Collection through Hot Carrier Extraction. *Nano Lett.* **2011**, *11*, 5426–5430.
23. Lin, C.; Tsai, F.-Y.; Lee, M.-H.; Lee, C.-H.; Tien, T.-C.; Wang, L.-P.; Tsai, S.-Y. Enhanced Performance of Dye-Sensitized Solar Cells by an Al_2O_3 Charge-Recombination Barrier Formed by Low-Temperature Atomic Layer Deposition. *J. Mater. Chem.* **2009**, *19*, 2999–3003.
24. O'Regan, B. C.; Scully, S.; Mayer, A. C.; Palomares, E.; Durrant, J. The Effect of Al_2O_3 Barrier Layers in TiO_2/Dye/CuSCN Photovoltaic Cells Explored by Recombination and DOS Characterization Using Transient Photovoltage Measurements. *J. Phys. Chem. B* **2005**, *109*, 4616–4623.
25. Kanter, H. Slow-Electron Mean Free Paths in Aluminum, Silver, and Gold. *Phys. Rev. B* **1970**, *1*, 522–536.
26. Sze, S. M. *Physics of Semiconductor Devices*, 2nd ed.; John Wiley & Sons: New York, 1981; p 868.
27. Shewchun, J.; Waxman, A.; Warfield, G. Tunneling in MIS structures—I. *Solid-State Electron.* **1967**, *10*, 1165–1186.
28. Huang, M. L.; Chang, Y. C.; Chang, C. H.; Lin, T. D.; Kwo, J.; Wu, T. B.; Hong, M. Energy-Band Parameters of Atomic-Layer-Deposition Al_2O_3/InGaAs Heterostructure. *Appl. Phys. Lett.* **2006**, *89*, 012903.
29. McCreery, R. L. Molecular Electronic Junctions. *Chem. Mater.* **2004**, *16*, 4477–4496.
30. Mihailetchi, V.; Wildeman, J.; Blom, P. Space-Charge Limited Photocurrent. *Phys. Rev. Lett.* **2005**, *94*, 126602.
31. Pattantyus-Abraham, A. G.; Kramer, I. J.; Barkhouse, A. R.; Wang, X.; Konstantatos, G.; Debnath, R.; Levina, L.; Raabe, I.; Nazeeruddin, M. K.; Grätzel, M.; *et al*. Depleted-Heterojunction Colloidal Quantum Dot Solar Cells. *ACS Nano* **2010**, *4*, 3374–3380.